

Three-dimensional quantum Hall effect in Weyl semimetals

Mingqi Chang,¹ Hao Geng,^{1,*} Li Sheng,^{1,2,†} and D. Y. Xing^{1,2}

¹*National Laboratory of Solid State Microstructures and Department of Physics, Nanjing University, Nanjing 210093, China*

²*Collaborative Innovation Center of Advanced Microstructures, Nanjing University, Nanjing 210093, China*



(Received 13 April 2021; accepted 23 June 2021; published 28 June 2021)

We analytically study the three-dimensional (3D) quantum Hall effect (QHE) in a thin film of a Weyl semimetal from the perspective of bulk states. We derive the Chern numbers for $B \neq 0$ from the Chern numbers for $B = 0$ through a topological analysis and obtain a phase diagram of Chern numbers in Weyl semimetals. We demonstrate how the relative alignment of the Weyl nodes and the thickness of the film influence the quantum Hall plateaus and predict a peculiar phase diagram for the QHE in a thin film of a Weyl semimetal. Our work reveals the nature of the 3D QHE in Weyl semimetals from the bulk states.

DOI: [10.1103/PhysRevB.103.245434](https://doi.org/10.1103/PhysRevB.103.245434)

I. INTRODUCTION

The Weyl semimetal, a new topological material with a nontrivial electronic structure, has attracted intense interests in condensed matter physics in the last decade [1–9]. In a Weyl semimetal, energy bands touch at discrete Weyl nodes which always occur in pairs with opposite chirality [10]. Near the Weyl nodes the band dispersion is approximated as being exactly linear, satisfying the Weyl equation, a two-component Dirac equation. A landmark feature of Weyl semimetals is the Fermi-arc surface state that connects the Weyl nodes with different chiralities in momentum space. The states of Fermi arcs are confined only in a region between the Weyl nodes because of the topological origin [11]. These unique features of Weyl semimetals produce many intriguing quantum transport properties, such as chiral anomaly [3,10,12,13], negative longitudinal magnetoresistance [14–16], and the planar Hall effect [17–20].

The quantum Hall effect (QHE), discovered in 1980 [21], is usually observed in two-dimensional (2D) systems [22–24] with a 1D edge states protected by topology [25]. It is well known that the observation of a 3D QHE is difficult because of the extra dimension along the magnetic field. However, recently, a 3D QHE was predicted to occur in Weyl semimetals [26–28]. Reference [26] proposes that Fermi arcs at opposite surfaces can form a complete Fermi loop and support the QHE via a “wormhole” tunneling assisted by the Weyl nodes. Meanwhile, this exotic quantum Hall phenomenon was observed experimentally in topological semimetals Cd_3As_2 , with thicknesses ranging from 10 to 80 nm under a magnetic field [29–35]. Recently, a numerical calculation shows that the sample size will affect the quantized plateaus of the 3D QHE in Weyl semimetals [36]. The present edge-state picture of 3D QHE cannot explain the effects of the sample size and the relative alignment of the Weyl nodes [26,37].

In this paper, we present an analytical study of the 3D QHE in the thin films of Weyl semimetals. We establish a bulk picture of 3D QHE from Landau levels which is more robust than the picture of surface states [26,37]. As a magnetic field is applied perpendicular to the film, we solve the Landau levels and derive the Chern numbers for $B \neq 0$ from the Chern numbers for $B = 0$ through a topological analysis and give the phase diagram of the Chern number in Weyl semimetals. We demonstrate that the quantized Hall conductivity is attributed to the zeroth chiral Landau levels traversing through the finite gap of $n = -1$ and $n = 1$ Landau levels. We exhibit how the relative alignment of the Weyl nodes and the thickness of the film influence the quantum Hall plateaus. A phase diagram for the QHE is predicted in a thin film of Weyl semimetals. We also derive a general formula of the Hall conductivity.

We organize this paper as follows. In Sec. II, we introduce a Weyl semimetal with two Weyl nodes and calculate the Chern numbers. We solve the Landau levels of the Hamiltonian in Sec. III, and in Sec. IV we demonstrate the phase diagram of Chern number in the presence of the magnetic field. We calculate the quantized Hall conductivity of the Weyl semimetals and predict a phase diagram for the QHE in Sec. V. The final section contains a summary.

II. MODEL

Let us consider a Weyl semimetal with two Weyl nodes. A minimal low-energy model of the electrons around a Weyl node is given by

$$H = \chi v_F (\mathbf{k} - \mathbf{k}_w^\chi) \cdot \boldsymbol{\sigma}, \quad (1)$$

where $\chi = +$ or $-$ represents the chirality of the Weyl node, v_F is the Fermi velocity, and $\boldsymbol{\sigma} \equiv (\sigma_x, \sigma_y, \sigma_z)$ are the Pauli matrices. We keep using the “absolute” momentum $\mathbf{k} \equiv (k_x, k_y, k_z)$ to describe the electron states for convenience of discussion. For definitiveness, we assume that the $\chi = \pm$ Weyl nodes are located at $\mathbf{k}_w^\pm \equiv (k_{wx}^\pm, k_{wy}^\pm, k_{wz}^\pm)$ in the momentum space. The displacement of the $\chi = +$ Weyl node from the $\chi = -$ Weyl node is denoted by $2\mathbf{k}_w \equiv 2(k_{wx}, k_{wy}, k_{wz}) =$

*genghao@nju.edu.cn

†shengli@nju.edu.cn

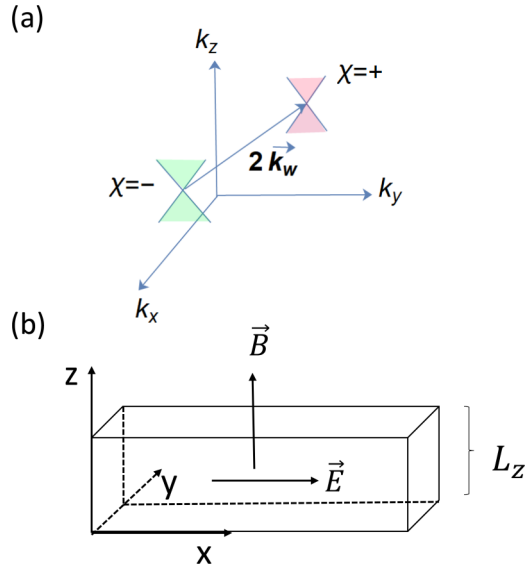


FIG. 1. Schematic illustration of (a) the two Weyl nodes in (k_x, k_y, k_z) space and (b) a thin film of a Weyl semimetal in (x, y, z) space with a magnetic field along the z direction and an electrical field along the x direction.

$\mathbf{k}_w^+ - \mathbf{k}_w^-$, which orients in an arbitrary direction in general, as illustrated in Fig. 1. The eigenenergies of this model are $E_{\mathbf{k}}^\chi = \pm v_F |\mathbf{k} - \mathbf{k}_w^\chi|$ with \pm for the conduction and valence bands.

To characterize the topological property of the Weyl semimetal, we regard k_z as a parameter, and calculate the Chern number $C(k_z)$ of all the occupied electron states in the k_x - k_y plane. If k_z does not coincide with the Weyl nodes, there always exists an energy gap between the conduction and valence bands. We assume that the Fermi energy is in the energy gap, and calculate the Chern number $C(k_z)$ for a given k_z . The Weyl nodes are the drain and source of the Berry curvature, and contribute to the Chern number, separately. The contribution from the Weyl node χ is easily obtained as $C_\chi(k_z) = -\chi/2$ for $k_z < k_{wz}^\chi$ and $C_\chi(k_z) = \chi/2$ for $k_z > k_{wz}^\chi$. The total Chern number $C(k_z) = C_+(k_z) + C_-(k_z)$ for a given k_z is then

$$C(k_z) = \begin{cases} -\text{sgn}(k_{wz}), & k_z \text{ between two Weyl nodes,} \\ 0, & \text{otherwise.} \end{cases} \quad (2)$$

The Chern number $C(k_z)$ vs k_z is shown in Figs. 2(a) and 2(c), for $k_{wz} < 0$ and $k_{wz} > 0$, respectively. We notice that the Chern number $C(k_z)$ has opposite signs in the two cases. If the Weyl nodes are located at a plane perpendicular to the z axis, such that $k_{wz} = 0$, the Chern number vanishes for all k_z , except at the Weyl nodes, where the Chern number is not defined. Our result is consistent with the previous theory of Chern numbers for Weyl semimetals [38].

III. LANDAU LEVELS

We now investigate how the electron states in the Weyl semimetal evolve in the presence of a magnetic field. Let us consider that a magnetic field $\mathbf{B} = (0, 0, B)$ is applied along the z axis. By using the Peierls substitution, the momentum

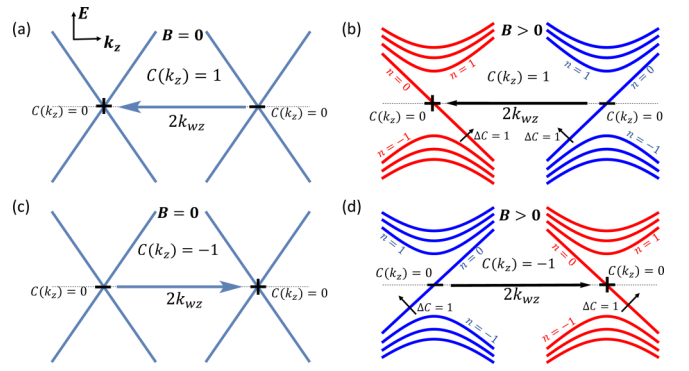


FIG. 2. Energy spectrum as a function of k_z for (a), (c) $B = 0$ and (b), (d) $B > 0$. In (a) and (b), $k_{wz} < 0$ is assumed, and in (d) and (c), $k_{wz} > 0$ is assumed. The Chern numbers $C(k_z)$ are labeled in the figure, and \pm denote the chiralities of the Weyl nodes.

is replaced by $\mathbf{k} \rightarrow (\mathbf{k} - q\mathbf{A})$, where \mathbf{A} is the vector potential and the electron charge is taken to be $q = -e$. In the Landau gauge, the vector potential is chosen to be $\mathbf{A} = (0, Bx, 0)$. Around the Weyl node χ , we introduce the ladder operators $a = l_B[(k_x - k_{wx}^\chi) - i(x - x_0)/l_B^2]/\sqrt{2}$ and $a^\dagger = l_B[(k_x - k_{wx}^\chi) + i(x - x_0)/l_B^2]/\sqrt{2}$, where $x_0 = -\text{sgn}(B)l_B^2(k_y - k_{wy}^\chi)$ is the guide center, and $l_B = \sqrt{\hbar}/|eB|$ is the magnetic length. The eigenenergies of the Landau levels (LLs) can be solved as

$$E_{n,k_z}^\chi = \begin{cases} -\chi v_F (k_z - k_{wz}^\chi) \text{sgn}(B), & n = 0, \\ \text{sgn}(n) |v_F| \sqrt{2|n|/l_B^2 + (k_z - k_{wz}^\chi)^2}, & n \neq 0. \end{cases} \quad (3)$$

The corresponding eigenvectors are

$$\Psi_{k_y, k_z}^{\chi, n=0} = \begin{bmatrix} 0 \\ \phi_{k_y, k_z}^{(0)} \end{bmatrix}, \quad B > 0, \quad (4)$$

$$\Psi_{k_y, k_z}^{\chi, n=0} = \begin{bmatrix} \phi_{k_y, k_z}^{(0)} \\ 0 \end{bmatrix}, \quad B < 0,$$

for $n = 0$, and for $n \neq 0$,

$$\Psi_{k_y, k_z}^{\chi, n} = \frac{1}{\sqrt{2}} \begin{bmatrix} \sqrt{1 + \zeta \cos \theta} \phi_{k_y, k_z}^{(|n|-1)} \\ \zeta \sqrt{1 - \zeta \cos \theta} \phi_{k_y, k_z}^{(|n|)} \end{bmatrix}, \quad B > 0, \quad (5)$$

$$\Psi_{k_y, k_z}^{\chi, n} = \frac{1}{\sqrt{2}} \begin{bmatrix} \zeta \sqrt{1 + \zeta \cos \theta} \phi_{k_y, k_z}^{(|n|)} \\ \sqrt{1 - \zeta \cos \theta} \phi_{k_y, k_z}^{(|n|-1)} \end{bmatrix}, \quad B < 0,$$

where $\theta = \arccos[(k_z - k_{wz}^\chi)/\sqrt{2|n|/l_B^2 + (k_z - k_{wz}^\chi)^2}]$, and $\zeta = \text{sgn}(n\chi)$. Here, $\phi_{k_y, k_z}^{(|n|)}(\mathbf{r})$ are the wave functions of electrons with ordinary parabolic dispersion in a magnetic field, given by

$$\phi_{k_y, k_z}^{(|n|)}(\mathbf{r}) = C_n e^{ik_y y + ik_z z} e^{-\frac{(x-x_0)^2}{2l_B^2}} \mathcal{H}_{|n|}\left(\frac{x-x_0}{l_B}\right), \quad (6)$$

where $C_n = 1/\sqrt{|n|!2^{|n|}\sqrt{\pi}L_y L_z l_B}$, $L_y L_z$ is the cross section of the sample in the y - z plane, and $\mathcal{H}_{|n|}$ is the Hermite polynomial. The Landau degeneracy is $N_L = 1/2\pi l_B^2 = eB/\hbar$ in a unit cross section in the x - y plane, as the electron eigenenergies do not depend on k_y .

IV. PHASE DIAGRAM OF CHERN NUMBER

In the presence of the magnetic field, k_z is still a good quantum number, and the energy spectrum of the electrons will evolve into many LL energy bands. We plot the LLs as functions of k_z in Figs. 2(b) and 2(d), for $k_{wz} < 0$ and $k_{wz} > 0$, respectively. The two chiral $n = 0$ LL bands go through the two Weyl nodes, respectively. The topological properties of the model can still be described by the Chern number $C(k_z)$ of all the occupied electron states. An interesting way to obtain the Chern number $C(k_z)$ for $B \neq 0$ is based on topological analyses. We consider (E_F, k_z) as a pair of variable parameters, which designates an observation point. Let us first focus on Figs. 2(a) and 2(b). At $B = 0$, we set $E_F = 0$ and k_z to be between the two Weyl nodes. When the magnetic field B is switched on continuously, while the electron energy spectrum evolves into different LL bands, no LL band crosses the observation point (E_F, k_z) . In other words, the observation point remains in an energy gap during the process. Therefore, the value of the Chern number at $B = 0$, $C(k_z) = 1$, at (E_F, k_z) cannot change with increasing the magnetic field B . Furthermore, in Fig. 2(b) because the whole region enclosed by the $n = 0$ and $n = 1$ LL bands is connecting to the observation point (E_F, k_z) , one can move (E_F, k_z) throughout the region without crossing any LLs. The whole region must share the same Chern number $C(k_z) = 1$ as indicated in Fig. 2(b).

A similar analysis can be applied to other regions. We now set $E_F = 0$ and k_z to the left of the left Weyl node at $B = 0$. When B is increased continuously to a finite value, because no LL band swiftly moves across the observation point (E_F, k_z) during the process, $C(k_z)$ at (E_F, k_z) will not change. As a result, we can determine that the Chern number in the region enclosed by the $n = 0$ and $n = -1$ LL bands in the left valley is $C(k_z) = 0$. For the same reason, $C(k_z) = 0$ in the region enclosed by $n = 0$ and $n = -1$ LL bands in the right valley. Apparently, in Fig. 2(b), if we move (E_F, k_z) from a $C(k_z) = 0$ region to the $C(k_z) = 1$ region, (E_F, k_z) must cross upwards from below an $n = 0$ LL. This indicates that each $n = 0$ LL carries a Chern number $\Delta C(k_z) = 1$, as indicated in the figure. The Chern numbers in different regions in Fig. 2(d) are determined in the same manner.

A special case is that the two Weyl nodes are located at the x - y plane, as shown in Figs. 3(a) and 3(b). The Chern number distribution for finite B can also be derived from the Chern number at $B = 0$. We may set our observation point $E_F = 0$ and k_z to the left of the Weyl points, and then continuously increase B from zero to a finite value. During this process, because no LL passes through the observation point, the Chern number at the observation point, $C(k_z) = 0$, remains unchanged. Therefore, the Chern number in the region between the $n = 0$ LL bands to the left of the Weyl points must be the same, i.e., $C(k_z) = 0$. The same argument is applicable to the region between the $n = 0$ LL bands to the right of the Weyl points. Furthermore, by considering that each $n = 0$ LL carries a Chern number $\Delta C(k_z) = 1$, we can decide immediately the Chern numbers in the regions between $n = 0$ LL bands and $n = \pm 1$ LL bands are $C(k_z) = \pm 1$, as indicated in Fig. 3(b).

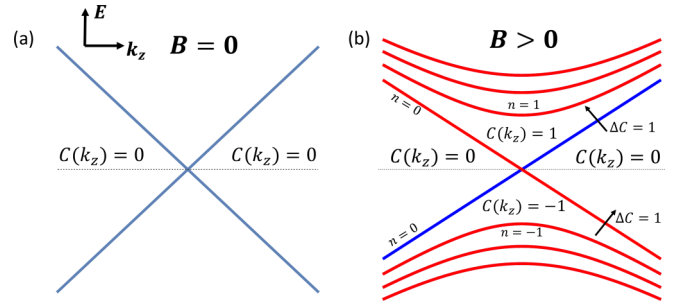


FIG. 3. Energy spectrum as a function of k_z for (a) $B = 0$ and (b) $B > 0$, when the Weyl nodes are separated in the x - y plane, namely, $k_{wz} = 0$. The Chern numbers $C(k_z)$ are labeled in the figure.

The above topological discussion can be directly verified by calculation of the Chern number carried by each LL. The easiest way to calculate the Chern number is based on the perturbation theory [16]. The presence of a weak electronic field E_x along the x direction introduces a small perturbation of potential energy to the system,

$$\Delta V = -eE_x x. \quad (7)$$

The eigenenergies of the LL states are corrected to $E_{n,k_z}^x - eE_x x_0$ because $\langle x \rangle = x_0$. The energy correction gives rise to a group velocity along the y direction,

$$v_y \equiv \frac{1}{\hbar} \frac{\partial (E_{n,k_z}^x - eE_x x_0)}{\partial k_y} = \frac{eE_x l_B^2 \text{sgn}(B)}{\hbar}. \quad (8)$$

It is interesting to notice that v_y is simply a constant for every LL state. Then the Chern number of each LL with degeneracy $1/2\pi l_B^2$ is given by

$$\Delta C(k_z) = \frac{1}{2\pi l_B^2} \frac{v_y \hbar}{eE_x} = \text{sgn}(B), \quad (9)$$

which is valid for any LL. For $B > 0$ and for the $n = 0$ LLs, the result $\Delta C(k_z) = 1$ is exactly consistent with the above topological discussion. Moreover, using this result we can further determine the Chern number in different regions, as indicated in Figs. 2(b) and 2(d). For $B < 0$, one can apply the same topological arguments to obtain the corresponding phase diagram, and verify that each LL carries a Chern number $\Delta C(k_z) = -1$, which is consistent with Eq. (9).

V. QUANTIZED HALL CONDUCTIVITY

We consider in general that the system thickness L_z is finite. If we employ a periodic boundary condition in the z direction, the wave vector k_z is discrete, given by $k_z = 2i\pi/L_z$ with i as an integer. When the electron Fermi energy is in an energy gap, the total Hall conductivity will be quantized in units of e^2/h ,

$$\sigma_{xy} = \nu \frac{e^2}{h}, \quad (10)$$

where $\nu = \sum_{k_z} C(k_z)$ is the total Chern number of all the occupied electron states below the Fermi energy.

At $B = 0$, the total Chern number does not vanish if the z component of the relative displacement is nonzero, i.e., $k_{wz} \neq 0$, as indicated by Eq. (2). We consider the simple case, where $E_F = 0$. The Chern number at $B = 0$ can be obtained as

$$\nu = -2 \text{Int} \left(\frac{k_{wz} L_z}{2\pi} \right) - \text{sgn}(k_{wz}), \quad (11)$$

where $\text{Int}(\dots)$ is to take the integer part of a real number. A nonzero quantized Hall conductivity in the absence of an applied magnetic field is well known as the quantum anomalous Hall (QAH) effect. The nonzero Chern number at $B = 0$ is responsible for the emergence of chiral Fermi-arc surface states connecting the projections on the surfaces in the x and y directions. The QAH effect can also be understood in terms of the surface states. However, we would like to point out that the quantization of the Hall conductivity at $B = 0$ is unstable in the presence of disorder, because the bulk of a Weyl semimetal is metallic at $B = 0$. An electron transition between the surface states and bulk states caused by disorder scattering is unavoidable, which will destroy the quantization of Hall conductivity.

For finite B , we focus on the energy region between the $n = -1$ and $n = 1$ LLs, whose width is about $2E_g = 2\sqrt{2}\hbar\omega_c$ with $\omega_c = v_F/l_B$ as the cyclotron frequency. In the energy region, the QHE is controlled only by the $n = 0$ LLs. Outside the energy region, multiple LL bands are overlapping, the energy gaps between neighboring LLs are usually small, and hence the QHE is relatively unstable. For electron Fermi energy in the energy region between the $n = -1$ and $n = 1$ LLs, the total Hall conductivity in units of e^2/h can be calculated by summing $C(k_z)$ over all allowable k_z , yielding

$$\nu = -2 \text{Int} \left(\frac{k_{wz} L_z}{2\pi} + \frac{\text{sgn}(B) E_F L_z}{2\pi \hbar v_F} \right) - \text{sgn}(k_{wz}). \quad (12)$$

In the $B \rightarrow 0$ limit, we notice that $E_g \rightarrow 0$. We may set $E_F = 0$, because Eq. (12) is valid only for E_F between $-E_g$ and E_g . Then we can find that Eq. (12) is consistent with Eq. (11).

In Fig. 4(a), we show the phase diagram of the Hall conductivity on the Fermi energy versus system thickness L_z plane for the case where the two Weyl nodes are aligned along the z direction. We see that the Hall conductivity is nonsymmetric about $E_F = 0$, and displays only odd-integer Hall plateaus. It is quantized at relative large integer numbers, essentially because of the extra contribution from the QAH. In Fig. 4(b), we plot the Hall conductivity as a function of E_F/E_g for three different values of system thickness. With increasing E_F , the Hall plateau increases incrementally by 2 each time, owing to the valley degeneracy. With increasing the system thickness L_z , more higher plateaus emerge within the energy region from $-E_g$ to E_g , but the plateau width decreases. This can be understood as follows. The spacing between two nearby discrete k_z is $2\pi/L_z$. Therefore, the energy spacing between two neighboring $n = 0$ LLs is given by $\Delta E = v_F^z \hbar (2\pi/L_z)$, being in inverse proportion to the thickness L_z , which determines the width of the quantized Hall plateaus. In addition, the narrower are the plateaus, the more plateaus will be seen in the energy region from $-E_g$ to E_g . The lowest and highest Hall plateaus can be determined by substituting $-E_g$ and E_g into Eq. (12).

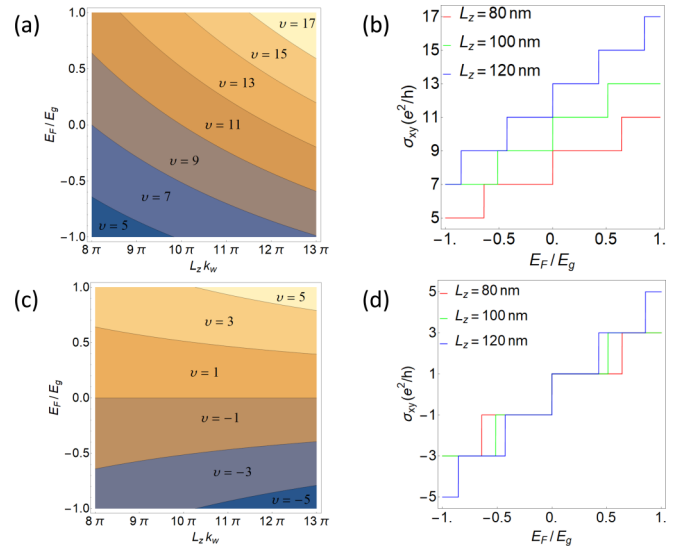


FIG. 4. (a), (c) Phase diagram for QHE on the E_F/E_g vs $L_z k_w$ plane, and (b), (d) quantized Hall conductivity in units of e^2/h as a function of E_F/E_g for some different values of sample thicknesses L_z . In (a) and (b), the Weyl nodes are separated along the z direction. In (c) and (d), the Weyl nodes are separated in the x - y plane. The parameters are $k_w = \pi/10 \text{ nm}^{-1}$, and $\mathbf{B} = (0, 0, 5T)$.

In Fig. 4(c), we show the phase diagram of the Hall conductivity on the Fermi energy versus system thickness L_z plane for the case where the two Weyl nodes are located in the x - y plane. We see that the Hall conductivity is antisymmetric about $E_F = 0$. The Hall conductivity is an odd function of E_F , as shown in Fig. 4(d). From Figs. 4(a)–4(d), we see that the Hall conductivity exhibits only odd-integer Hall plateaus. Taking into account the valley degeneracy $g = 2$, we may write

$$\nu = g \left(n + \frac{1}{2} \right), \quad (13)$$

with n as an integer, which is reminiscent of the half-integer quantized QHE in graphene. Such an interesting quantization rule is attributable to the π Berry phase shift at the Weyl points, similar to that at the Dirac points in graphene.

The finite system thickness L_z is necessary. When the thickness L_z is small, the QHE plateaus with finite width will emerge. The plateau width of Hall conductivity will be too narrow to be observed when the thickness L_z is large.

VI. SUMMARY

In summary, we analytically investigate the 3D QHE in a thin film of a Weyl semimetal. As a magnetic field is applied perpendicular to the film, we solve the Landau levels and we derive the Chern numbers for $B \neq 0$ from the Chern numbers for $B = 0$ through a topological analysis. A peculiar phase diagram for the QHE is predicted in the Weyl semimetals. We demonstrate how the relative alignment of the Weyl nodes and the thickness of the film influence the quantum Hall plateaus. We also derive a general formula of the Hall conductivity. As proposed in Ref. [2], a two-Weyl-node Weyl semimetal

can be realized in a multilayer heterostructure consisting of alternating layers of a 3D topological insulator and an ordinary insulator, and such a multilayer has been experimentally realized [39]. Our methods and results are anticipated to be verified in such a Weyl semimetal.

ACKNOWLEDGMENTS

This work was supported by the State Key Program for Basic Researches of China under Grant No. 2017YFA0303203 (D.Y.X.), and the National Natural Science Foundation of China under Grants No. 11674160 and No. 11974168 (L.S.).

-
- [1] X. Wan, A. M. Turner, A. Vishwanath, and S. Y. Savrasov, *Phys. Rev. B* **83**, 205101 (2011).
- [2] A. A. Burkov and L. Balents, *Phys. Rev. Lett.* **107**, 127205 (2011).
- [3] K. Y. Yang, Y. M. Lu, and Y. Ran, *Phys. Rev. B* **84**, 075129 (2011).
- [4] G. Xu, H. Weng, Z. Wang, X. Dai, and Z. Fang, *Phys. Rev. Lett.* **107**, 186806 (2011).
- [5] P. Delplace, J. Li, and D. Carpentier, *Europhys. Lett.* **97**, 67004 (2012).
- [6] J.-H. Jiang, *Phys. Rev. A* **85**, 033640 (2012).
- [7] B. Singh, A. Sharma, H. Lin, M. Z. Hasan, R. Prasad, and A. Bansil, *Phys. Rev. B* **86**, 115208 (2012).
- [8] J. Liu and D. Vanderbilt, *Phys. Rev. B* **90**, 155316 (2014).
- [9] D. Bulmash, C.-X. Liu, and X.-L. Qi, *Phys. Rev. B* **89**, 081106(R) (2014).
- [10] H. Nielsen and M. Ninomiya, *Phys. Lett. B* **130**, 389 (1983).
- [11] S.-B. Zhang, H.-Z. Lu, and S.-Q. Shen, *New J. Phys.* **18**, 053039 (2016).
- [12] M. M. Vazifeh and M. Franz, *Phys. Rev. Lett.* **111**, 027201 (2013).
- [13] S. A. Parameswaran, T. Grover, D. A. Abanin, D. A. Pesin, and A. Vishwanath, *Phys. Rev. X* **4**, 031035 (2014).
- [14] D. T. Son and B. Z. Spivak, *Phys. Rev. B* **88**, 104412 (2013).
- [15] A. A. Burkov, *Phys. Rev. Lett.* **113**, 247203 (2014).
- [16] H.-Z. Lu, S.-B. Zhang, and S.-Q. Shen, *Phys. Rev. B* **92**, 045203 (2015).
- [17] A. A. Burkov, *Phys. Rev. B* **96**, 041110(R) (2017).
- [18] S. Nandy, G. Sharma, A. Taraphder, and S. Tewari, *Phys. Rev. Lett.* **119**, 176804 (2017).
- [19] J. Yang, W. L. Zhen, D. D. Liang, Y. J. Wang, X. Yan, S. R. Weng, J. R. Wang, W. Tong, L. Pi, W. K. Zhu, and C. J. Zhang, *Phys. Rev. Mater.* **3**, 014201 (2019).
- [20] N. Kumar, S. N. Guin, C. Felser, and C. Shekhar, *Phys. Rev. B* **98**, 041103(R) (2018).
- [21] K. v. Klitzing, G. Dorda, and M. Pepper, *Phys. Rev. Lett.* **45**, 494 (1980).
- [22] K. S. Novoselov, A. K. Geim, S. V. Morozov, D. Jiang, M. I. Katsnelson, I. V. Grigorieva, S. V. Dubonos, and A. A. Firsov, *Nature (London)* **438**, 197 (2005).
- [23] Y. Zhang, Y.-W. Tan, H. L. Stormer, and P. Kim, *Nature (London)* **438**, 201 (2005).
- [24] R. Yoshimi, K. Yasuda, A. Tsukazaki, K. S. Takahashi, N. Nagaosa, M. Kawasaki, and Y. Tokura, *Nat. Commun.* **6**, 8530 (2015).
- [25] D. J. Thouless, M. Kohmoto, M. P. Nightingale, and M. den Nijs, *Phys. Rev. Lett.* **49**, 405 (1982).
- [26] C. M. Wang, H.-P. Sun, H.-Z. Lu, and X. C. Xie, *Phys. Rev. Lett.* **119**, 136806 (2017).
- [27] H.-Z. Lu, *Nat. Sci. Rev.* **6**, 208 (2019).
- [28] H.-P. Sun and H.-Z. Lu, *Front. Phys.* **14**, 33405 (2019).
- [29] C. Zhang, A. Narayan, S. Lu, J. Zhang, H. Zhang, Z. Ni, X. Yuan, Y. Liu, J.-H. Park, E. Zhang, W. Wang, S. Liu, L. Cheng, L. Pi, Z. Sheng, S. Sanvito, and F. Xiu, *Nat. Commun.* **8**, 1272 (2017).
- [30] B.-C. Lin, S. Wang, S. Wiedmann, J.-M. Lu, W.-Z. Zheng, D. Yu, and Z.-M. Liao, *Phys. Rev. Lett.* **122**, 036602 (2019).
- [31] F. Tang, Y. Ren, P. Wang, R. Zhong, J. Schneeloch, S. A. Yang, K. Yang, P. A. Lee, G. Gu, Z. Qiao, and L. Zhang, *Nat. Commun.* **569**, 537 (2019).
- [32] C. Zhang, Y. Zhang, X. Yuan, S. Lu, J. Zhang, A. Narayan, Y. Liu, H. Zhang, Z. Ni, R. Liu, E. S. Choi, A. Suslov, S. Sanvito, L. Pi, H.-Z. Lu, A. C. Potter, and F. Xiu, *Nature (London)* **565**, 331 (2019).
- [33] M. Uchida, Y. Nakazawa, S. Nishihaya, K. Akiba, M. Kriener, Y. Kozuka, A. Miyake, Y. Taguchi, M. Tokunaga, N. Nagaosa, Y. Tokura, and M. Kawasaki, *Nat. Commun.* **8**, 2274 (2017).
- [34] S. Nishihaya, M. Uchida, Y. Nakazawa, M. Kriener, Y. Kozuka, Y. Taguchi, and M. Kawasaki, *Sci. Adv.* **4**, eaar5668 (2018).
- [35] T. Schumann, L. Galletti, D. A. Kealhofer, H. Kim, M. Goyal, and S. Stemmer, *Phys. Rev. Lett.* **120**, 016801 (2018).
- [36] R. Ma, D. N. Sheng, and L. Sheng, *arXiv:2008.13431*.
- [37] H. Li, H. Liu, H. Jiang, and X. C. Xie, *Phys. Rev. Lett.* **125**, 036602 (2020).
- [38] P. Hosur and X. Qi, *C. R. Phys.* **14**, 857 (2013).
- [39] G. Jiang, Y. Feng, W. Wu, S. Li, Y. Bai, Y. Li, Q. Zhang, L. Gu, X. Feng, D. Zhang, C. Song, L. Wang, W. Li, X.-C. Ma, Q.-K. Xue, Y. Wang, and K. He, *Chin. Phys. Lett.* **35**, 076802 (2018).